AIAA SciTech Forum
6-10 January 2020, Orlando, FL
AIAA Scitech 2020 Forum

10.2514/6.2020-2045

The Lift Force Produced by an Unsteady Translating Plate with a Rotating Tip

Juhi Chowdhury*, Cameron Smith† and Matthew J. Ringuette‡
University at Buffalo, the State University of New York, Buffalo, NY 14260 USA

Dynamic effects of wing planform changes are investigated with the goal of gust alleviation. Force measurements are done on a low-aspect-ratio, high-angle-of attack translating wing having a rectangular planform that further incorporates a moving tip with in-plane rotation and sweep. The wing is towed in a water tank with various velocity ramps starting from a constant motion, which are categorized as step-up (increasing velocity) and step-down (decreasing velocity); ramps over distances of 1, 3, and 6 chords traveled are used for both types of gusts. The tip panel is rotated inward for step-up cases with an aim to lower the gust lift peaks, and similarly rotated outward for step-down gusts to reduce the negative force change. The forces from the actuation cases are compared with those of two reference geometries corresponding to pre- and post-gust wing shapes, namely rectangular and static-sweep where the tip panel is fully retracted or extended, respectively. Further, the sensitivity of the actuation effects to aspect ratio ($\mathcal{AR}$) is examined. The lift coefficient, C_L, uses the instantaneous main-wing translation velocity and the varying wing area to compare across all cases. The step-up gust C_L resembles that of the starting flow for the 1-chord ramp, as reported by others. The step-down gusts exhibit a C_L minimum then an increase to a circulatory-force peak. For both gust types, apart from the 6-chord step-up case, when the C_L curves are aligned at 50% of the gust-ramp travel, the post-gust circulatory peaks coincide. For the step-up gusts and tip-panel actuation out, the $\mathcal{AR} = 2$ case yields a more substantial C_L reduction (gust mitigation) but it is not sustained compared to the $\mathcal{AR} = 4$ actuation effect. Wingtip actuation at the 50% gust location produces a more sustained, lower C_L but does not affect the gust peak, while actuation before the peak for the longer ramp cases reduces the peak value but the mitigation effect is not prolonged. For the step-down gusts, actuation out is effective at increasing the C_L. For $\mathcal{AR} = 4$ the effect is greatest for the 1-chord ramp and yields a C_L plateau between the gust minimum and recovery peak that is higher than for $\mathcal{AR} = 2$. However, for the longer deceleration ramps the $\mathcal{AR} = 2$ actuation-out case produces relatively larger actuation peaks and earlier gust recovery.

I. Introduction

THE goal of the present work is to test whether a moving wingtip surface that employs in-plane rotation and sweep can aid in mitigating the lift changes from simplified step-up and step-down streamwise gusts. The rotating tip surface, referred to here as a tip panel, dynamically changes the wing planform. The panel is deployed on a low-aspect-ratio translating wing at high angle of attack (α). The long-term application of this research is to develop a method of flow control for unmanned aerial vehicles (UAVs) to employ for maneuvers or gust alleviation.

For wings in unsteady translation at high α, dynamic stall will occur for which the flow separates and a leading-edge vortex (LEV) forms that yields large lift then sheds [1, 2]. Tip effects occur for wings of finite aspect ratio ($\mathcal{AR}$), and Taira and Colonius [3] performed numerical simulations to examine $\mathcal{AR} = 1$–4 translating wings at large α starting from rest and undergoing long travel distances. They showed that tip vortex (TV) downwash lowers the wing lift coefficient, C_L, an effect which progresses as the $\mathcal{AR}$ becomes smaller and the TV influence increases. At $\mathcal{AR} = 1$, the LEV remains attached due to the dominant TVs, but for higher $\mathcal{AR}$ this is only true near the wingtips and the inboard LEV lifts off into an arch shape and sheds. Jardin *et al.*[4] similarly found that the TV promotes LEV attachment, for simulations of flapping wings in translation. For further recent work on the forces and flow structure for finite-$\mathcal{AR}$ wings in unsteady translation, see Stevens *et al.*[5] which covers results from the NATO AVT-202 group. Here we consider $\mathcal{AR} = 2$ and 4 wings to ensure that inboard LEV shedding will occur, and observe how the moving tip panel may alter the flow.

*Ph.D. Student, Department of Mechanical & Aerospace Engineering, 211 Bell Hall, Buffalo NY 14260, AIAA Student Member.
†Undergraduate Student, Department of Mechanical & Aerospace Engineering, 211 Bell Hall, Buffalo NY 14260.
‡Associate Professor, Department of Mechanical & Aerospace Engineering, 211 Bell Hall, Buffalo NY 14260, AIAA Member.

For wings in unsteady, pure rotation, several studies have shown that the LEV is attached for low local Rossby number (Ro), also in the context of TV and $\mathcal{AR}$ effects, e.g. Refs. [6–11]. The low-$\mathcal{AR}$ rotating tip panel examined here is superimposed on the main-wing translation, for which the advance ratio J incorporating wing translation and rotation is also important. Sect. II.C discusses this and leverages the rotating-wing study of Harbig *et al.*[12] for varying J.

The moving tip panel studied here incorporates aft sweep as it rotates. For unswept translating rectangular wings the LEV and TV are distinct [13, 14], but although sweep and the spanwise flow it produces do not alone yield LEV attachment, sweep can facilitate an LEV-TV connection [15]. For low-$\mathcal{AR}$ translating wings, swept and curved planforms also cause the LEV and TV to connect, which yields outboard vorticity transport, and delays both the LEV shedding and peak C_{L} [3]. However, for a wing in translation with added flapping (lateral rotation about the root), which produces a spanwise vorticity gradient, sweep can enhance spanwise flow and aid in LEV attachment [16, 17]. Numerical simulations by Jardin and David [18] also showed that although a spanwise velocity gradient across the wing span can alone promote LEV attachment, for wing rotation the LEV is closer to the wing and generates larger lift. van Oorschot *et al.*[19] performed tests on actual bird wings with either fixed, aft sweep outboard or the sweep reduced and area increased by extending the wing, done in a freestream flow or for steady revolving. Sweep produces a larger $C_{\mathrm{L,max}}$ at a higher α in the freestream flow, but for revolving the extended wings generate greater C_{L}.

Recently, Hayostek *et al.*[20] experimentally investigated unswept and swept $\mathcal{AR} = 2$ and 6 wall-mounted wings in a water channel using dye visualization and S-PIV. They identified tip, wake, and wall regions, which for $\mathcal{AR} = 2$ have overlap and affect one another, but for $\mathcal{AR} = 6$ the end influences are more isolated. Aft sweep introduces outboard spanwise flow, which lowers the TV strength, and the flow separation and vortex shedding are substantially lessened. A follow-on direct-numerical-simulation study by Zhang *et al.*[21], using instead a root symmetry-plane condition, showed a persistent TV for all configurations with strength most affected by α, and that tip effects lower the performance versus 2-D cases. In addition, periodic shedding of spanwise vortices was found for $\mathcal{AR} = 4$, and for $\mathcal{AR} = 6$ a vortex "dislocation" was discovered in the shedding region closer to the symmetry plane. Between the tip and spanwise shedding is a region of slanted, zig-zag "interaction vortices" which have the same shedding frequency as the spanwise structures. Such structures, although more diffuse, are also visible in our longer-time dye visualizations [22]. Also, Medina *et al.*[23] used experiments and computations to investigate the dynamic stall of a 30°-swept wing with a semi-span $\mathcal{AR} = 2$, but sinusoidal pitching about 1/4-chord. An arch vortex was observed inboard of the TV which unpins, then connects with the TV itself as the TV unpins, leading to full tip stall.

Static tip sweep was also examined by Nicolic [24] and Lee and Pereira [25], who employed half delta-wing, i.e. swept, tip shapes also referred to as strakes. Depending on the main-wing and strake orientations, the results showed increased C_{L} and maximum lift-to-drag ratio, likely due to strake vortex lift. Although this research was done for lower $\alpha < 25°$ and a steady freestream versus the high-α, unsteady conditions of the present work with variable tip geometry, it shows that such tip shapes can improve performance.

The proposed paper uses a rotating tip geometry, and prior work has also been done on dynamically-changing wing shapes. For example, Reynolds *et al.*[26] showed that a steppe eagle quickly lowers ("tucks") its wings below its body in response to a headwind gust followed by some disturbance like a downdraft that produces a drop in lift. The tucking is likely the response of muscle tension to a suddenly reduced wing loading, but they speculate that it could also be a mechanism for damping the gust perturbation. Wang *et al.*[27] used DNS to study slow-flying bats, and showed that a dynamic increase in wingspan during flapping, compared to a fixed-span case, produces greater lift and efficiency by enhancing the LEV strength, in addition to the effect of the larger wing area. Returning to birds, Harvey *et al.*[28] examined freely-gliding gulls and cadaver wings in wind tunnels, and demonstrated that variations in wing elbow angles, which alter the camber and aerodynamic center, could vary the bird's static pitch stability. For additional discussions on the forelimb adaptations of bat and bird wings and potential inspiration for robotic drones, see Ref. [29].

Considering more simplified engineering approaches, building off the work of Wibawa *et al.*[30], Steele *et al.*[31] investigated the fast spanwise retraction of vertically mounted wings towed at constant-α in a water tank. The square-tip wing (emulating a "vanishing body") creates spanwise vortices and a vortex ring that makes the wake unstable, the square but hollow tip ("melting body") requires less energy to retract than the first since it does not produce further momentum in the spanwise direction and is more favorable for flow control, while the rounded tip ("shrinking body") generates weaker spanwise vortices and results in added-mass energy recovery and thrust. Recently Scofield *et al.*[32] studied LEV vorticity transport control for an $\mathcal{AR} = 3$ flat-plate wing translating from rest, via a tip that bends dynamically in the suction direction by 35°. Experiments using PIV indicated that at 80% span the LEV circulation growth and shedding are delayed, and DNS demonstrated that the bending increases spanwise vorticity convection.

Di Luca *et al.*[33] designed and fabricated a bird-inspired morphing wing with the left and right outboard portions each consisting of multiple artificial feathers, which when fully extended produce outboard sweep, or by rotation inboard

with overlap the feathers can fold the wing to decrease the span and lower the area by 41%. From wind tunnel tests measuring time-averaged forces, they showed that the expanded wing provides greater C_L and maneuvering capability, while retraction reduces the drag coefficient for higher speed. Also, installing the wings on a drone, they demonstrated that asymmetric actuation can be used for roll control. This variable wing geometry shares similarities with that of the present study, however we employ a rigid wingtip panel and examine the unsteady forces and flow.

Regarding streamwise gusts, here the focus is on simple non-periodic changes in velocity. Recent experiments have shown that using a moving model with respect to a constant (or zero) freestream velocity to produce a gust-like interaction is equivalent to employing a stationary wing in a wind tunnel having time-varying freestream velocity changes, provided that the buoyancy effects from this accelerating freestream and the wing-model inertial loads for the moving-wing case are accounted for [34–36]. Mulleners *et al.*[37] conducted experiments on an $\alpha = 30°$ flat-plate wing, and compared the LEV and TEV development and C_L decay for: 1) starts from rest and 2) a streamwise acceleration from a fully-developed state at constant velocity to a final velocity 50% higher than the initial wing velocity. They found that after the initial startup, both cases are similar in terms of time-varying flow and C_L variations and decay. Marzanek and Rival [38] studied a non-slender delta-wing at $\alpha = 20°$ and $30°$ accelerating from rest in a freestream to a new speed that is 50% faster, to emulate a headwind gust, via constant acceleration over $1c$–$6c$. For $\alpha = 30°$, they found sensitivity to the acceleration rate: e.g. for the $1c$ case, it exhibits high sustained C_L associated with a favorable pressure gradient and flow separation with subsequent reattachment.

Initial work on the present wing configuration was done using qualitative dye flow visualization with an $\mathcal{AR} = 6.8$ wing in a water towing-tank facility [22]. This $\mathcal{AR}$ value is twice that of the vertically-submerged wing, excluding the tip panel, accounting for the reflected free-surface boundary condition. The wing was a flat plate in unsteady translation with $\alpha = 45°$ and a Reynolds number of $Re = 10,000$. Tests included a starting flow with outward panel actuation, meant to increase lift, and a 50% 1/2-sine streamwise gust (surge) at 21 chords ($21c$) traveled with inward panel rotation, intended to shed the panel's leading or swept-edge vortex (SEV) and promote inboard LEV shedding to reduce the gust lift increase. The azimuthal speed of the panel's tip was a factor of 1.49 greater than the main-wing translation speed. For the starting flows, outward panel rotation at $0.1c$ traveled generates a panel SEV, stretches the TV and trailing-edge vortex (TEV) outboard and upstream, and displaces the adjacent LEV outboard; these behaviors should increase the lift. By comparison, the SEV for a reference case with panel fixed in its extended, swept position is not as closely attached. For both moving and fixed-panel configurations, the outboard LEV entrains the SEV vorticity and weakens it for a time. Starting the panel actuation at $1.3c$ traveled has a reduced effect, because the LEV is stronger when the actuation begins, as is its entrainment of the SEV flow. The gust tests showed that panel retraction causes shedding of the SEV and local TEV, consistent with the vanishing-body case of Steele *et al.*[31], and as desired yields LEV shedding similar to the rectangular wing that is more pronounced than in the fixed-sweep case. Moreover, the moving panel produces an inboard shift of the TV flow, which should lower the lift.

The objective of the current paper is to build on this prior work and quantitatively examine how the moving panel affects the C_L. The same water towing-tank is used with a force transducer to measure the wing lift. Two main questions are considered: 1) To what level can the increased lift due to a streamwise, headwind gust be reduced via inward panel rotation? 2) How effective is outboard panel rotation at mitigating the lift lost during a streamwise, tailwind gust? To address (1) and (2), simple "step-up" and "step-down" streamwise gusts are tested, starting from a constant velocity and accelerating or decelerating, respectively, to a new constant velocity. The parameters varied include the gust acceleration duration, the panel actuation timing, and the main-wing $\mathcal{AR}$; $\mathcal{AR}$s of 2 and 4 are studied, to ensure inboard LEV shedding but reduce the entrainment effect from the strong LEV found for $\mathcal{AR} = 6.8$. The moving-panel results are compared to two reference cases having fixed planforms at the extremes of the panel actuation: the main wing with no tip panel deployed ("rectangular" wing), and a fixed tip panel fully extended outward with constant sweep ("static sweep" case).

II. Experimental Setup and Methods

A. Facility and Wing Model

The facility is a 4 m × 1.5 m × 1.1 m glass-walled towing tank with water as the working fluid (Fig. 1a). It is open at the top, and the bottom and side walls are supported by a steel frame which elevates it 1 m for imaging from underneath. Above the tank is a further frame of extruded-aluminum beams, and four cross beams support a 3 m long brushless linear stage (H2W Technologies DRS-120-08-006-01-EX) for towing models. A tray is installed adjacent to the stage which supports the cable bundle attached to the stage's carriage, plus the cabling for the wingtip actuation motor, providing smooth cable travel as the carriage moves. A Galil DMC4040 controller employing encoder feedback

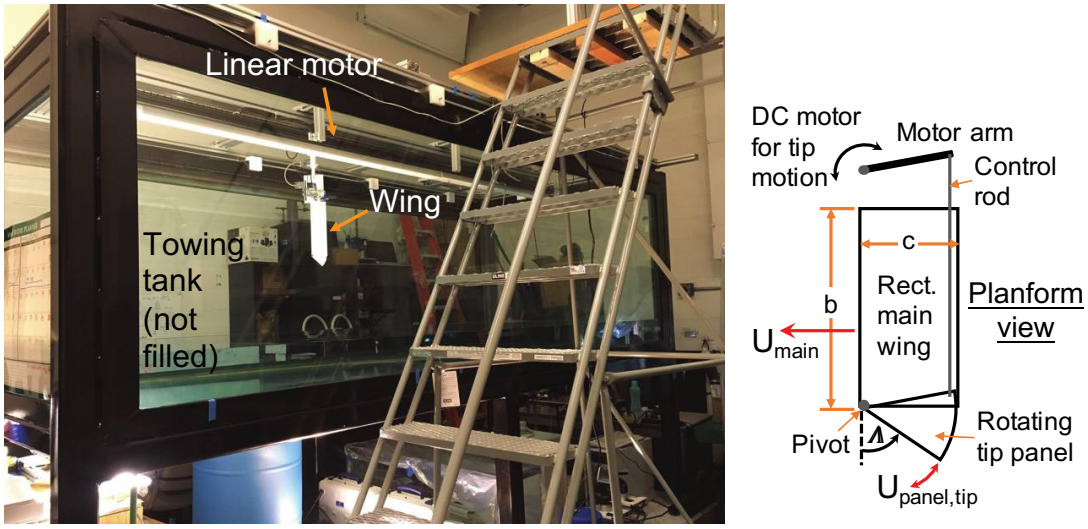

Fig. 1 Experimental setup. (a) Towing-tank facility, indicating the wing and linear motor. (b) Schematic of the wing, giving the tip-panel actuation scheme, wing geometry, and wing velocities.

provides programmable motion profiles for the linear stage and the tip-panel actuation. The coordinated motions are developed and carried out using Galil Design Kit software. The position accuracy of the linear-stage encoder is rated at 1 micron, however maximum deviations of about 100 microns, or ~0.1%c, occur during the gust motions.

The main wing is made from two carbon-fiber composite sheets of thicknesses 3.18 mm and 0.79 mm, with a chord length of $c = 81$ mm. A cavity is machined out of the thicker plate to allow room for the actuation mechanism and retracting tip panel; the two plates are glued together with marine epoxy to form the complete wing with 3.97 mm thickness. The rotating tip panel is a 1.59 mm thick carbon-fiber composite plate cut into an approximately 1/8-circle shape, the apex of which is pivoted at the leading edge and tip corner of the main wing via a binding barrel. The tip panel is rotated via a small motor above the free surface, called the tip motor (brushed DC servo motor, Micromo model 2642W012CXRIE3-1024L+26A 16:1+MG26, with 65536 encoder counts per revolution), that is mounted on an aluminum plate which also supports the main wing.

The panel motion is accomplished as follows (see Fig. 1b). A stainless-steel control rod connects to an arm collared on the tip-motor shaft; the rod/arm connection is a rotational joint. The rod passes down through the wing cavity, and connects at its lower end to the aft/inboard corner of the pivoted tip panel, also with a rotational joint. The control rod connection to the arm is 68.6 mm from the center of the tip-motor axle, which is approximately the same distance between the tip-panel pivot point and its connection to the rod. Therefore the panel rotates with the tip motor via the rod, with a nearly one-to-one conversion. Some part of the tip panel is always inside the main wing even when fully extended; the exposed panel has an average radius of 73 mm from the exposed panel apex. The sweep angle between a line parallel to the main-wing leading edge (LE) and the panel LE is Λ (Fig. 1b), and the angle between the tip edge of the rectangular main wing and the panel LE is $(90^\circ - \Lambda)$. Using the latter angle, 46.72° of motor rotation yields 45° of exposed tip rotation. The tip panel can completely retract into the main wing ($\Lambda = 90^\circ$), or fully extend giving $\Lambda = 45^\circ$. The panel rotational velocity is verified using 240 frame-per-second movies of the panel motion. The angular position of its LE over time is determined from still images using Gimp software. The manual edge-finding incurs some error, but shows that the average angular panel velocity from the images is within 0.3% of the motor velocity.

B. Force Measurements

The lift force is measured using a 6-axis ATI Gamma force/torque sensor attached between the linear-stage carriage plate and the wing's sting support. The transducer's negative y-direction is aligned with the wing's lift direction. The Gamma signals are acquired with a 16-bit National Instruments DAQ card (PCIe-6323) via LabVIEW, and sampled at 1 kHz after receiving a trigger signal from the motion controller. For each case, $N = 10$ runs are taken in water and in air; the latter allow the model inertial forces to be subtracted off, leaving the fluid-dynamic forces of interest. MATLAB

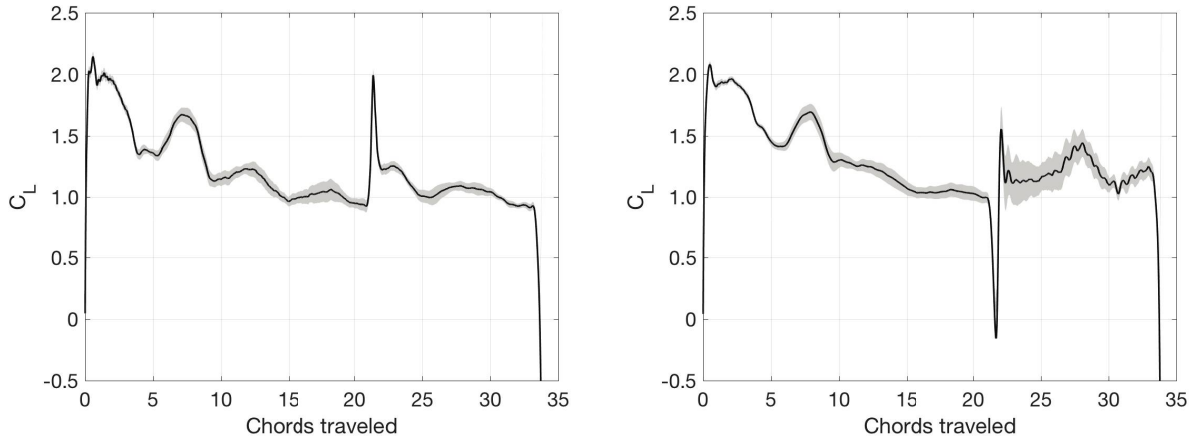

Fig. 2 Plots showing the filtered C_L from the mean of 10 runs in water with the average of 10 runs in air subtracted off (black line), and the corresponding precision error calculated as described in the text (gray band). Note that the instantaneous U_{main} and wing area are used in calculating the C_L, which make the pre- and post-gust values more comparable. The cases are the $\mathcal{AR} = 4$ wing for: (a) the $1c$ step-up gust with tip-panel actuation-in at $21.5c$ traveled and (b) the $1c$ step-down gust with panel actuation-out at the same distance traveled.

is used for data processing, and the mechanical vibrations and noise of the system are analyzed from strike tests as well as air and water runs by estimating the power spectral density. A 3rd-order Butterworth filter with a 4 Hz cutoff frequency is applied to the data which retains the flow-related forces while removing most of the vibration contributions. After filtering, all runs are aligned in time via a correlation, the air and water runs are separately averaged, then the air results are subtracted out.

The Gamma uses the ATI SI-32-2.5 calibration, and its accuracy is checked using static tests with precision weights for forces of ~0.2–2 N, covering the range of the experiment; the results are within 1.5% of the calibration. For a given case, the random uncertainty in the average lift coefficient, $\delta C_L(t)$, is computed at each time instance using the precision error of the mean from the run-to-run variations of the water measurements, $\delta C_{L,water}(t) = t_{\nu,0.95}\sigma_{water}(t)/\sqrt{N}$, and that of the air measurements, $\delta C_{L,air}(t) = t_{\nu,0.95}\sigma_{air}(t)/\sqrt{N}$, where $t_{\nu,0.95}$ is the Student's t-distribution for a 95% confidence level with $N-1$ degrees of freedom, and the sample standard deviation is σ. Overall, the mean lift coefficient and its precision error for each case are $\overline{C}_L(t) \pm \delta C_L(t) = (\overline{C}_{L,water}(t) \pm \delta C_{L,water}(t)) - (\overline{C}_{L,air}(t) \pm \delta C_{L,air}(t))$. Figure 2 shows two $\mathcal{AR} = 4$ cases with tip-panel actuation, the step-up and step-down gust with the gust acceleration or deceleration occurring over $1c$ of travel. For the step-up gust, actuation-in starts at $21.5c$ traveled, and for the step-down gust actuation-out begins at the same distance. These were chosen since they are representative of the whole measurement set. The gray band in each plot shows the precision-error bounds, and note that for the mean C_L the overline is omitted and implied from this point forward and in all plots. Also, in computing C_L the instantaneous U_{main} and wing area are employed, which yield more similar values before and after the gust. The precision error is overall lowest in the initial $Re = 18,000$ portion of the step-down gust, and highest after the step down to $Re = 9,000$ where the data have more variation and the signal is smallest. For the cases shown in Fig. 2, the time-average of the precision error in the mean C_L over the full motion duration is ±4% (±0.05) and ±6.7% (±0.08) for the step-up and step-down gusts, respectively.

C. Experimental Parameters

The main rectangular wing is oriented vertically through the free surface, which acts as a reflected (symmetry) boundary condition [30, 39]. For the rectangular wing with the tip panel fully retracted, the physically-submerged aspect ratio is $\mathcal{AR} = b/c$, set by varying the water level, where b is the wing span. Submerged $\mathcal{AR} = 1$ and 2 are used for the rectangular-wing portion, doubled to 2 and 4 by the reflection; all $\mathcal{AR}$s reported are the reflected values. The C_L for the reflected $\mathcal{AR} = 2$ and 4 cases is similar to available starting-flow data from the NATO RTO task group AVT-202 for fully-submerged wings of the same $\mathcal{AR}$s [5], supporting the reflected-boundary assumption. The main-wing Reynolds number ($Re = U_{main}c/\nu$), where ν is the kinematic viscosity and U_{main} is the translational velocity of the main wing, is

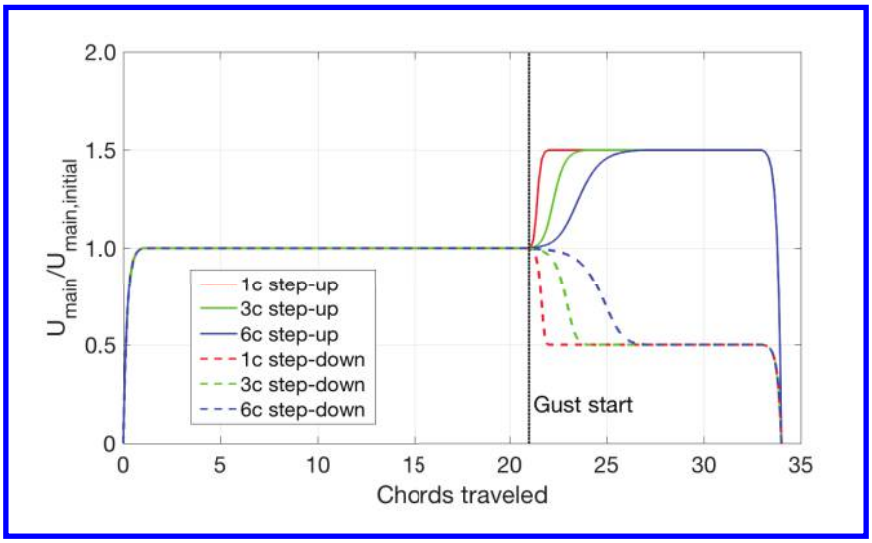

Fig. 3 Main-wing motion profiles for the step-up and step-down gust cases.

of order 10,000 or slightly below this for all cases. This is appropriate for small UAVs [40], and yields sufficiently-high signals from the force sensor. The C_L at $Re = 12,000$, which exhibits minimal free-surface deformations, matches that at the maximum $Re = 18,000$ tested within the error, for which the free-surface disturbances are somewhat larger particularly in the vortex cores, but otherwise small compared to the wing span. This indicates that adverse free-surface effects are not substantial over the Re-range tested. The angle of attack of the main wing is $\alpha = 45°$, chosen to produce flow separation with strong vortices, and due to the substantial prior work at this value. At $\alpha = 45°$, $\mathcal{AR} = 4$ and with the tip panel extended, the blockage ratio (submerged frontal-projected wing area divided by the filled tank cross-sectional area) is only ~1%.

The main-wing motions tested are simplified streamwise gust-like profiles, each having parameters varied; the tip-panel actuation is described below. Similar to Mulleners *et al.*[37] and Marzanek and Rival [38] we examine "step-up" gusts, but also "step-down" gusts. Using a moving model with respect to a constant (or zero) freestream velocity to produce a gust-like interaction has been shown to be equivalent to employing a stationary test article in a time-varying freestream, provided that the buoyancy effects from this accelerating freestream are accounted for [34–36]. Marzanek and Rival [38] point out that this has so far only been tested using nominally 2-D bodies (airfoils), however parameter variations using 3-D bodies in either configuration will produce insightful trends. The step-up and step-down cases can be thought of as emulating head-wind and tail-wind gusts, respectively. The gust cases all begin with acceleration from rest over $1c$ to constant $U_{\text{main,initial}}$, using a hyperbolic-tangent profile to mitigate mechanical vibrations. The hyperbolic-tangent curve is scaled to have the same average acceleration and duration as a constant-acceleration (linear) profile. At $21c$ traveled, the wing executes an additional acceleration to a higher constant velocity of $1.5U_{\text{main,initial}}$ for step-up gusts or deceleration to $0.5U_{\text{main,initial}}$ for step-down. Therefore the gust amplitude is 50% in each case, as for the step-up gusts of Mulleners *et al.*[37] and Marzanek and Rival [38]. Hyperbolic-tangent velocity profiles are also used during the acceleration and deceleration portions of the gust motions until the desired constant velocity is reached. The gusts are initiated after $20c$ so startup effects are not prominent, since the C_L approximately levels off to a low value and the wing exhibits more periodic LEV and TEV shedding (based on our prior flow visualization [22]). Greater than $30c$ may be ideal [37, 41], which could depend on $\mathcal{AR}$ and Re, however the present tank length cannot accommodate this. Similar to the step-up study of Marzanek and Rival [38], acceleration/deceleration or "ramp" distances of $1c$, $3c$, and $6c$ before the wing reaches the final step-up/step-down velocity, respectively, are tested. After $12c$ of travel beyond the gust start to observe the response, the wing decelerates and stops at a distance of $34c$.

Figure 3 shows the dimensionless wing velocity profiles versus chords traveled, nondimensionalized by $U_{\text{main,initial}}$. The Re values for the force measurements are a balance between ensuring sufficient sensor signals in the final phase for the step-down gust, and limiting the wing velocity to mitigate free-surface deformations for the initial portion of the step-down gust and last phase of the step-up gust. For the step-up and step-down cases, the constant velocity before/after the gust has $Re = 12,000/18,000$ and $Re = 18,000/9,000$, respectively. Reynolds-number effects on C_L in this range have been shown to be minimal [42] and are not the focus of the present study.

Table 1 Cases tested for the step-up/step-down gust motions for $\mathcal{AR} = 2$ and 4; the Reynolds numbers are given in the text.

Gust type	Gust accel./decel. dist.	Tip conditions tested
50% step-up gust	$1c$	Rect., static sweep ($\Lambda = 45°$), actuation-in at $21.5c$
at $21c$ traveled	$3c$	Rect., static sweep ($\Lambda = 45°$), actuation-in at $21.5c$ & $22.5c$
	$6c$	Rect., static sweep ($\Lambda = 45°$), actuation-in at $21.5c$ & $24.0c$
50% step-down gust	$1c$	Rect., static sweep ($\Lambda = 45°$), actuation-out at $21.5c$
at $21c$ traveled	$3c$	Rect., static sweep ($\Lambda = 45°$), actuation-out at $21.5c$ & $22.5c$
	$6c$	Rect., static sweep ($\Lambda = 45°$), actuation-out at $21.5c$ & $24.0c$

The goal of this paper is to examine whether the tip-panel actuation can mitigate the lift change produced by the step-up/step-down gusts. However, as indicated in Sect. I the aim here is to understand the panel's effect and not to do flow control or lift optimization. Inward rotation ("actuation-in") is employed to reduce the lift after the step-up gust, while outward rotation ("actuation-out") is used to increase the post-gust lift for the step-down case. For the former, the starting and ending values of Λ are 45° and 90°, while these are swapped for the latter. Chowdhury *et al.*[22] showed that actuation timing can substantially affect the flow structures, and here it is varied to study its influence on the lift. For all $1c$–$6c$ step-up/step-down acceleration/deceleration ramps, two actuation timings are tested: 1) early actuation at $21.5c$ of travel, i.e. early shortly after the gust initiation at $21c$, and 2) actuation at 50% of the travel distance during the ramp, namely at $21.5c$, $22.5c$, and $24c$ traversed for the $1c$, $3c$, and $6c$ ramp, respectively; for the $1c$ ramp the two timings are the same. The wing area and $\mathcal{AR}$ will vary for each case. With the panel retracted ($\Lambda = 90°$), the $\mathcal{AR}$ cases are simply the rectangular values of 2 and 4. For the fully-extended tip panel with $\Lambda = 45°$, the $\mathcal{AR}$ increases to 4.1 and 6, respectively, with corresponding increases in wing area of 31.7% and 15.8%. As mentioned earlier, two reference cases with the same U_{main} profiles but fixed tip geometries are tested for comparison: 1) the "rectangular" case with the tip panel fully-retracted (final geometry for actuation-in), and 2) the "static sweep" case where the tip panel is extended to $\Lambda = 45°$ (final geometry for actuation-out). Table 1 summarizes the motion cases.

The tip-panel motion is in addition to U_{main}, and is characterized using the advance ratio, J. For flapping-wing flight [43], typically J is taken as the forward velocity divided by the absolute value of the average azimuthal (rotational) wingtip velocity (excluding the superimposed translational velocity). Harbig *et al.*[44] studied LEV dynamics for rotating wings with a horizontal stroke plane in constant forward motion. For the downstroke, they created a J vs. $\mathcal{AR}$ diagram to show which values yielded a "stable" (mainly attached) or "unstable" (shed) LEV. The present tip panel has a tilted 45° rotational stroke plane, and to better compare with Harbig *et al.*[44] the component of the forward velocity in the plane of rotation, $U_{\text{main}} \cos\alpha$, is used similar to the definition for helicopters with a tilted rotor plane [45]. Further, since the panel does not rotate outward past $\theta = 45°$ its LE never achieves orthogonality with U_{main} as an insect wing typically does, so a factor of $\cos\Lambda$ is used to obtain the component of $U_{\text{main}} \cos\alpha$ orthogonal to the LE, i.e. parallel to the panel's chord direction. The final expression is $J = U_{\text{main}} \cos\alpha \cos\Lambda / U_{\text{panel,tip}}$. For all cases, the tip-panel motion profile is trapezoidal with constant acceleration and deceleration occurring over the first and last 10% of the duration, respectively, having constant $U_{\text{panel,tip}}$ in between; the rotational amplitude is always 45° giving $\Lambda = 45°$. The maximum, constant $U_{\text{panel,tip}}$ is used in the J formula. The constant-velocity magnitude for all cases, whether inward or outward panel rotation, is $U_{\text{panel,tip}} = 1.5 U_{\text{main,initial}}$. The U_{main} changes during wing acceleration/deceleration for step-up/step-down gusts, with the largest value being for the 50% step-up profiles that yields a maximum advance ratio of $J = 0.5$; this is the maximum J for all cases tested. For outward panel rotation, from extrapolation of the Harbig *et al.*[44] diagram for the $\mathcal{AR} \approx 1$ of the tip panel, $J \leq 0.5$ should produce an attached LEV (here SEV). The effective angle of attack for the 3-D tip-panel flow cannot be determined without quantitative velocity data, however our prior [22] flow visualization indicates the formation of an attached SEV for outward rotation, showing consistency with the results of Harbig *et al.*[44]; for inward panel actuation, our earlier study [22] found that the panel vortex system sheds.

Harbig *et al.*[44] and Lentink and Dickinson [6] also describe the role of *Ro* for a rotating wing in forward motion, concluding that if *Ro* is small, i.e. for short radial distances, LEV attachment can occur for low J. For rotating wings in hover, attached LEVs have been reported for approximately $Ro \leq 1.5$, using $Ro = r_g/c$, with r_g being the radius of gyration [6, 8]. Considering instead the local radial distance from the axis of rotation, attached LEVs have been found

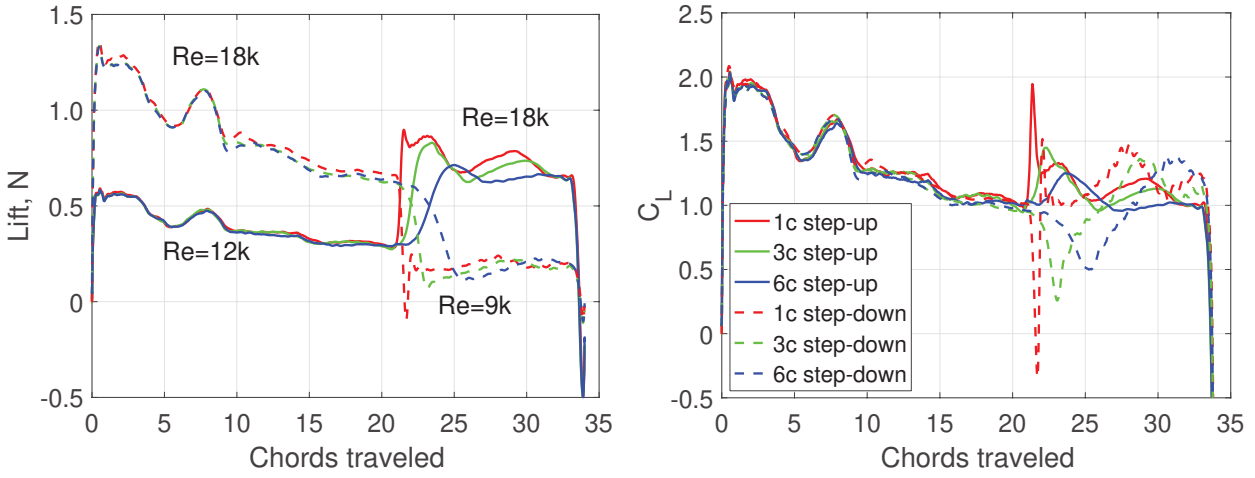

Fig. 4 Force measurements for the $\mathcal{AR} = 4$ rectangular-wing cases: (a) dimensional forces with Reynolds numbers before and after the gust motion labeled for the step-up and step-down gusts, and (b) C_L incorporating the instantaneous main-wing velocity, U_{main}. All gusts start at $21c$ of wing travel.

for about $r/c < 3$–4 for small root cutouts (offsets) for wing rotation in hover [7, 10, 46]. Several recent papers have shown the importance of having low *Ro* for LEV attachment and large lift, and how the effects of $\mathcal{AR}$ can be isolated from *Ro* and/or *Re*, with Refs. [9–11, 46] being representative. The tip panel's small $\mathcal{AR}$ should also have a sufficiently low *Ro* for SEV attachment, which our earlier flow visualization showed [22], as mentioned above.

III. Results

The results from the force measurements are presented here. First the rectangular reference case is used to show the key features of the step-up and step-down gust motions without tip-panel actuation, next the actuation cases are covered.

A. Rectangular Wing

Figure 4a gives the dimensional lift force, L, for the $\mathcal{AR} = 4$ rectangular step-up and step-down gust cases, to show their behavior prior to calculating C_L. For the starting-flow portion with acceleration from rest over $1c$, all curves exhibit an initial peak due to fluid-inertial (added-mass) force and circulatory force from the vortex growth. This is followed by a second peak (after acceleration ceases) due to vortex formation and shedding, and then a third, lower peak corresponding again to a formation and shedding cycle. Mulleners *et al.*[37] describe the interactions with the prior flow structures which cause this last, prominent circulatory peak to be reduced. This behavior is similar to that of the fully-submerged $\mathcal{AR} = 4$ starting-flow cases from the NATO AVT-202 study, as reported in Stevens *et al.*[5]. Consistent with the 50% step-up gust study of Mulleners *et al.*[37], here the qualitative lift trends for the $1c$-acceleration starting flow and $1c$ step-up gust resemble one another.

Figure 4b shows the corresponding C_L plot. The C_L is defined using the instantaneous main-wing velocity, U_{main}, from Fig. 3, so that the time-varying U_{main} is accounted for and any remaining C_L features can be attributed to unsteady flow phenomena. This gives $C_L = 2L/(\rho U_{main}^2 S)$, where ρ is the fluid density and S is the wing area. For the initial $1c$ startup acceleration, the C_L is instead nondimensionalized using the constant-velocity value just after acceleration, $U_{main,initial}$, since starting-flow scaling is not the focus of this paper. The C_L curves for $Re = 12,000$ and $Re = 18,000$ prior to the gust collapse very well, as expected given the *Re* independence mentioned above. Further, Fig. 4b indicates that using the instantaneous U_{main} for C_L makes the pre- and post-gust values more comparable. Considering the $1c$ step-down case (red dashed curve), just after the gust there is a negative force peak from the added-mass contribution followed by a brief positive peak; the C_L scaling increases their relative magnitudes versus the dimensional lift. The positive peak could be the continuation of the reducing circulatory-force value through the gust after the added-mass force ceases (see Fig. 4a), or just mechanical backlash. Further tests on the relative behavior of this second peak at

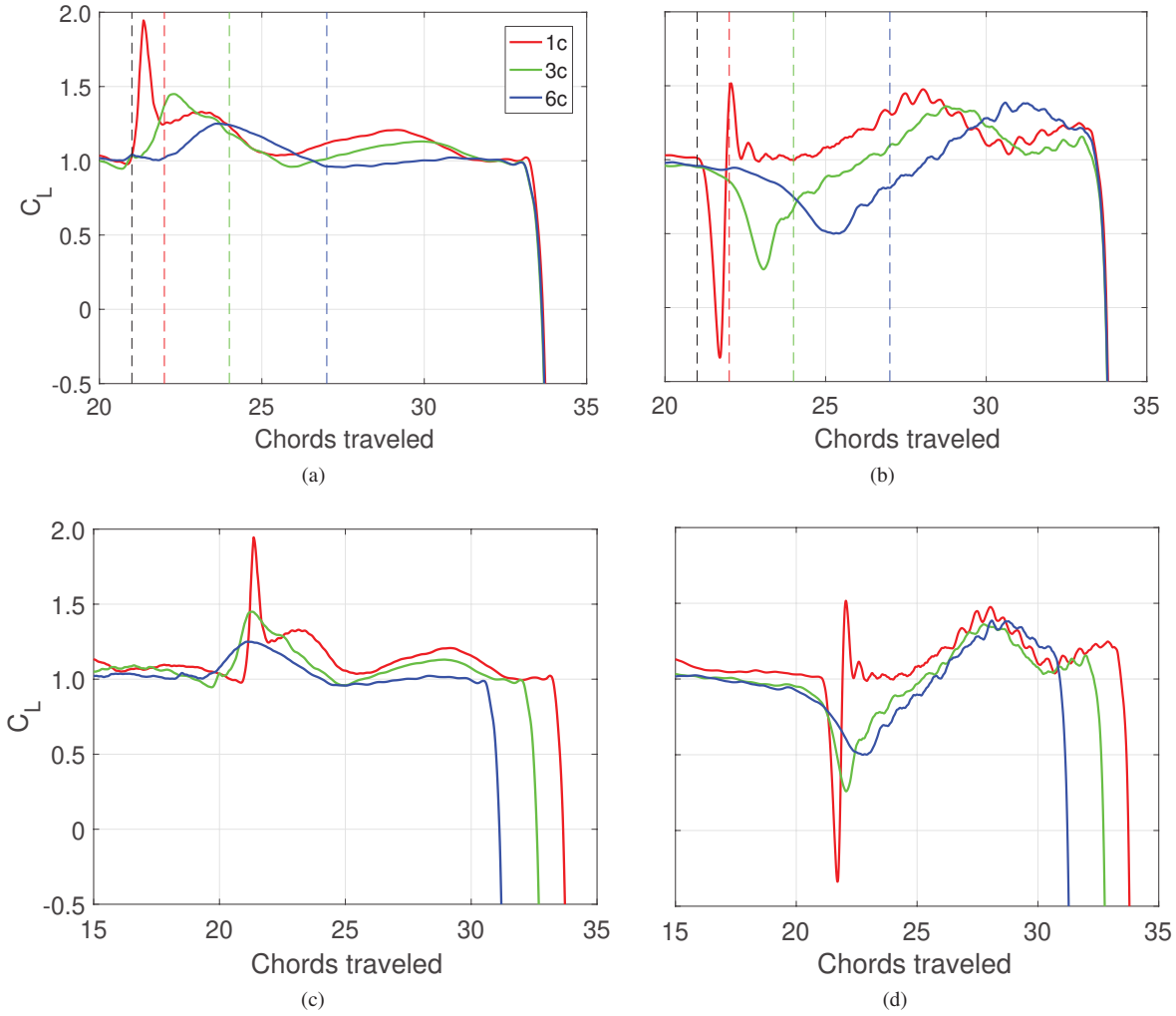

Fig. 5 Lift coefficients for the $\mathcal{AR} = 4$ rectangular-wing cases, focusing on the gust portion of the wing motion. (a) Step-up gusts, (b) step-down gusts, (c) step-up gusts with the $3c$ and $6c$ cases having the chords traveled shifted backward by half the gust acceleration distance, i.e. by $1.5c$ and $3c$, and (d) step-down gusts with the $3c$ and $6c$ results also shifted backward by the same respective values of chords traveled. The C_L incorporates the instantaneous main-wing velocity, U_{main}. The black dashed vertical line indicates the start of each gust at $21c$ traveled, whereas the colored dashed vertical lines designate the end of the gust acceleration or deceleration, with the colors corresponding to the gust distances in the legend.

different speeds are needed to determine the cause.

Figures 5a,b focus on the gust forces for the rectangular step-up and step-down cases. For the step-up gust, the $1c$ acceleration ramp yields a sharp initial peak with contributions from both added-mass and circulatory force, followed by two progressively lower and broader circulatory-lift peaks (Fig. 5a). For the $3c$ ramp the added-mass and initial circulatory-lift produce only a single peak, followed by a second, lower circulatory-force maximum. The $6c$ step-up gust also generates a single, broad first peak with the same contributions as that for the $3c$ ramp, but there is only a very weak second circulatory-force maximum that lies within the experimental error.

For the step-down gust, the $1c$-ramp case exhibits a $C_L < 0$ peak during maximum deceleration, and the $3c$ and $6c$ ramps also each show a clear C_L minimum, but with $C_L > 0$, corresponding to their maximum deceleration (Fig. 5b); the magnitudes of these minima are progressively smaller with greater deceleration distance. During deceleration the prior wake produced by the wing must impinge on it, be deflected by the wing, and likely widen; this is detrimental for lift production. Note that the magnitudes of the C_L minima for the step-down gusts, relative to the C_L prior to the gust initiation, are larger than those of the related positive peaks for the step-up cases. This may be caused by a greater added-mass force from the step-down wake impingement versus that from acceleration for the step-up case, however there is no way to determine this without quantitative flow data. For the step-down gusts, after the C_L minima as the deceleration gives way to the slower constant-velocity motion, all cases show a C_L recovery (increase) to a positive circulatory-force maximum.

For Figs. 5c,d, the chords traveled for the $3c$ and $6c$ gusts are shifted backward by half the gust width, i.e. $1.5c$ and $3c$ for the $3c$ and $6c$ gusts, respectively, for both the step-up and step down types. This shift yields an improved collapse of the step-up gust cases in terms of the timing of the $1c$ added-mass dominated peak and the first peaks for the $3c$ and $6c$ accelerations, and for the second circulatory peaks of the $1c$ and $3c$ gusts (Fig. 5c); however, the overall collapse is not very good. For the step-down gusts, the shift brings the low C_L peaks closer in terms of chords traveled as expected (Fig. 5d). However, they do not line up perfectly because the greatest deceleration does not occur exactly at 50% in terms of chords traversed, but rather at 50% of the total deceleration duration in time. The C_L recovery after the minimum shows a much better collapse via the shift, with the $3c$ and $6c$ cases being very close for nearly the full increase and peak afterward. The $1c$ gust instead shows a C_L plateau after the brief positive (backlash) peak, but beyond $\sim 25c$ traveled it collapses with the other two cases. The broad C_L peak after each gust finishes must be due to circulatory lift, and all peaks have similar magnitudes to e.g. the first circulatory peak of the $1c$ step-up gust case.

B. Tip-Panel Actuation and Aspect-Ratio Effects

Figures 6 and 7 show the step-up gust cases including tip-panel actuation-in and step-down gust results with actuation-out, respectively. They also compare data for $\mathcal{AR} = 4$ (top row) and 2 (bottom row); recall that the $\mathcal{AR}$ refers to the rectangular portion of the wing. Per Sect. II.C, actuation occurring at $21.5c$ is tested for all acceleration/deceleration gust ramps, as well as "50% actuation" which is done at the midpoint of the gust in terms of chords traveled. The 50% actuation happens at $22.5c$ and $24c$ traveled for the $3c$ and $6c$ gusts, respectively, and is the same as the $21.5c$-actuation timing for the $1c$ gust. For the tip-panel actuation cases, the C_L versus time incorporates both the instantaneous U_{main} for the velocity scale and the time-varying wing area. This again ensures that any deviations from the rectangular and static-sweep reference cases can be attributed to unsteady flow phenomena.

For the step-up gusts with actuation-in (Fig. 6), the wing starts in the static-sweep condition, then after actuation the tip panel is fully-retracted to the rectangular-wing case. Considering $AR = 4$, for the $1c$ ramp actuation-in at $21.5c$ (50% actuation) is too late to affect the added-mass dominated initial peak, but appreciably reduces both circulatory peaks compared to the static reference cases. A lower C_L from actuation versus the rectangular case indicates a truly unsteady-flow effect that cannot be accounted for by simply using the instantaneous wing area (and translating-wing velocity) in defining C_L. The flow visualization results of Chowdhury *et al.*[22] indicate that a key contributor to this C_L reduction is likely the shedding of the panel SEV-TV-TEV loop as the panel quickly retracts into the wing. Note that in between the circulatory peaks ($\sim 25.5c$ traveled), presumably after the main-wing vortex system sheds, the C_L for all $1c$-ramp cases is nearly the same. The overall C_L-reduction effect from inward actuation lasts for the remainder of the measurement, at least $12.5c$ traveled beyond the gust. The 50% actuation-in for the $3c$ ramp also does not affect the first peak C_L magnitude, but just after this the actuation lowers the C_L below that of the reference cases for the rest of the motion, except again near the local minimum where shedding occurs. For the $6c$ gust, the 50% actuation timing also reduces the C_L between the first peak and shedding, although the effect is slightly smaller, after which the actuation-in case is similar to the reference geometries except for a slight C_L decrease again near the end of the motion. The $21.5c$ actuation-in for the $3c$-ramp reduces the peak C_L during the gust, but afterward the C_L nearly matches the reference

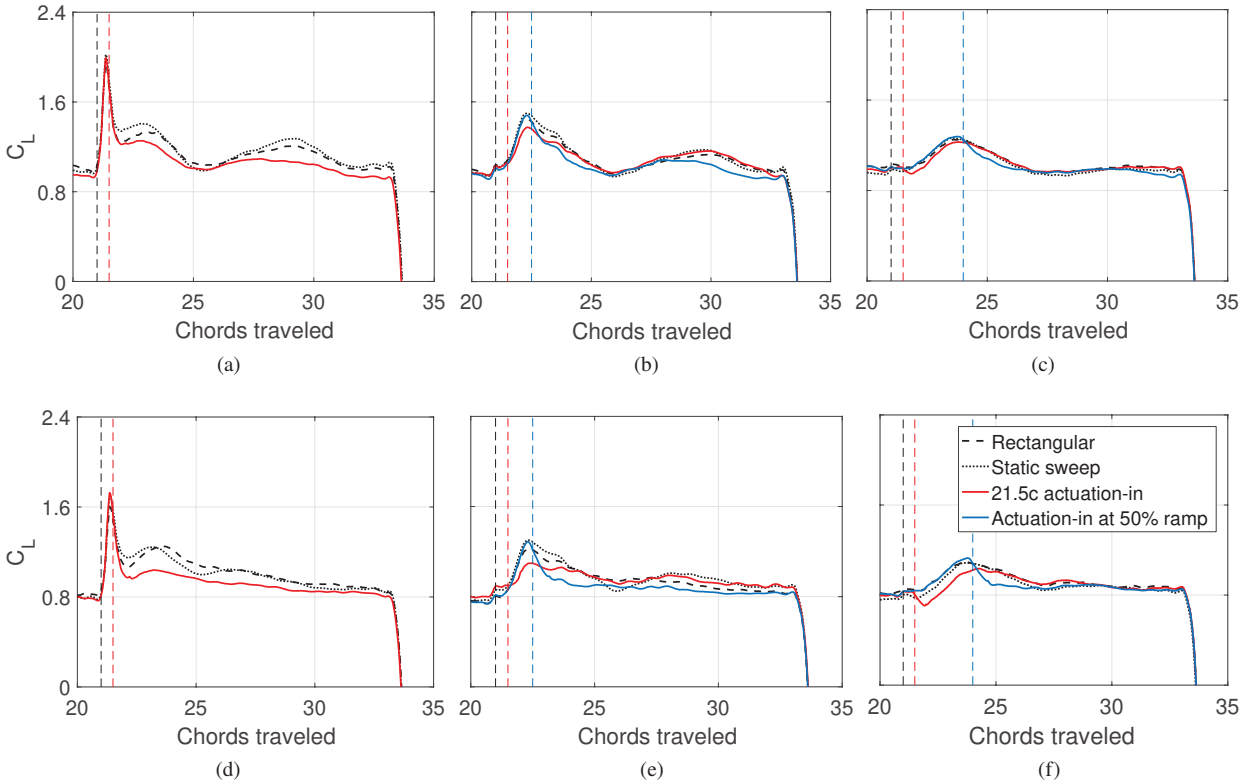

Fig. 6 Results for the step-up gust cases with tip-panel actuation-in for $\mathcal{AR} = 4$ (top row) and $\mathcal{AR} = 2$ (bottom row). (a,d), (b,e), and (c,f) show the $1c$, $3c$, and $6c$ gusts, respectively. The cases for each C_L curve are given by the legend, corresponding to the rectangular, static-sweep, and various actuation-in timings. The black dashed vertical line marks the start of all gusts at $21c$ traveled, and the red and blue dashed vertical lines indicate the initiation of the tip-panel actuation at $21.5c$ traveled and 50% of the ramp, respectively, per the legend colors. The 50%-ramp actuation (same as the red dashed line for the $1c$-gust, blue dashed line for $3c$ and $6c$) occurs at a distance traversed that is half-way through the gust acceleration, i.e. at $21.5c$, $22.5c$, and $24c$ for the $1c$-, $3c$-, and $6c$-gust, respectively. The C_L is defined using the instantaneous U_{main} as the velocity scale and a wing area equal to that of the main wing plus the instantaneous exposed tip-panel area.

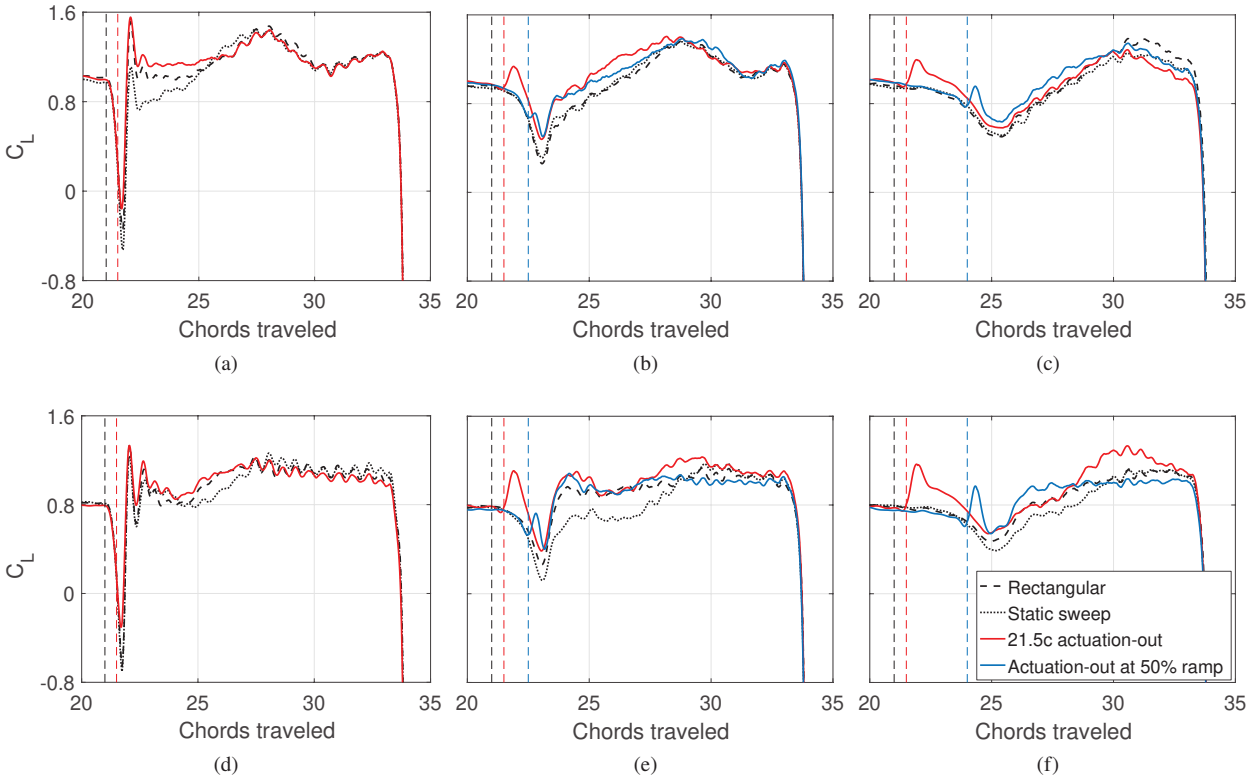

Fig. 7 Results for the step-down gust cases with tip-panel actuation-out for $\mathcal{AR} = 4$ (top row) and $\mathcal{AR} = 2$ (bottom row). (a,d), (b,e), and (c,f) show the $1c$, $3c$, and $6c$ gusts, respectively. The cases for each C_L curve are given by the legend, corresponding to the rectangular, static-sweep, and various actuation-out timings. The black dashed vertical line marks the start of all gusts at $21c$ traveled, and the red and blue dashed vertical lines indicate the initiation of the tip-panel actuation at $21.5c$ traveled and 50% of the ramp, respectively, per the legend colors. The 50%-ramp actuation (same as the red dashed line for the $1c$-gust, blue dashed line for $3c$ and $6c$) occurs at a distance traversed that is half-way through the gust deceleration, i.e. at $21.5c$, $22.5c$, and $24c$ for the $1c$-, $3c$-, and $6c$-gust, respectively. The C_L is defined using the instantaneous U_{main} as the velocity scale and a wing area equal to that of the main wing plus the instantaneous exposed tip-panel area.

cases. For the 6c-ramp and 21.5c actuation, the C_L curve is essentially the same as those of the reference wings. This does not mean that the moving panel has no effect on the dimensional lift, but rather that its effect can be scaled to be similar to the reference cases by also including the instantaneous wing area in the C_L. Overall, the 50% actuation timing has the greatest and most sustained C_L-reduction effect, being most pronounced for the 1c ramp and only slight for the 6c gust, but it is too late to influence the gust peak itself for the 1c ramp and the initial gust-peak value for the 3c and 6c ramps.

The corresponding $\mathcal{AR} = 2$ step-up gust cases are shown in the second row of Fig. 6. Compared to $\mathcal{AR} = 4$, the C_L curves for $\mathcal{AR} = 2$ have an overall lower magnitude, consistent with the smaller $\mathcal{AR}$. For the 1c and 3c ramps, for $\mathcal{AR} = 2$ a second circulatory-force peak is not present in almost all cases, except where a slight maximum exists for the static-sweep geometry, whereas this feature is prominent for $\mathcal{AR} = 4$. Considering that the step-up gust shows similarities with starting flows, this is consistent with the starting-flow $\mathcal{AR}$ trends from Stevens *et al.*[5] and Taira and Colonius [3]. The latter study showed less-pronounced C_L peaks from vortex shedding for $\mathcal{AR} = 2$ versus 4 at $\alpha = 40°$ due to the greater effect of downwash from the wingtip vortices.

Overall, actuation-in for $\mathcal{AR} = 2$ produces a larger change in C_L magnitude (with respect to the reference cases) during and shortly after the gust compared to $\mathcal{AR} = 4$, which is expected given that the extended $\mathcal{AR} = 2$ tip panel has a relatively greater percentage of the total wing area. However, this change is related to a dynamic flow effect, since the variable wing area is accounted for in C_L. This $\mathcal{AR}$ difference occurs for the 1c-ramp actuation-in case during the first circulatory-force peak, and for the 3c-ramp with 21.5c actuation which has a relatively lower gust peak and with 50% actuation where the post-gust C_L is smaller compared to the reference geometries. Also, for the 6c ramp the 21.5c and 50% actuation-in cases yield measurably lower C_L before and after the peaks for the reference cases, respectively, which is not found for $\mathcal{AR} = 4$. However, for $\mathcal{AR} = 2$ the panel's actuation effect is less sustained for the 1c- and particularly 3c-ramp cases versus $\mathcal{AR} = 4$; for the 3c ramp the actuation influence is negligible after 25c of travel. This may be related to the lack of a prominent, second circulatory force peak for $\mathcal{AR} = 2$, perhaps indicating that for $\mathcal{AR} = 4$ the moving panel's performance is enhanced by an interaction with the expected stronger inboard LEV formation, and its shedding; further quantitative flow information is needed to explore this.

Figure 7 gives the actuation-out cases for the step-down gusts. The wing begins with the rectangular geometry then the tip panel rotates outward to have the static-sweep planform. For $\mathcal{AR} = 4$ (top row), overall the actuation increases the C_L compared to the reference cases both during and after the gust, depending on the ramp length. The most pronounced effect is for the 1c ramp, for which the magnitude of the negative C_L peak is reduced substantially and the post-gust C_L plateau is higher than the reference cases. The flow visualization of Chowdhury *et al.*[22], albeit for a starting flow, shows an SEV forming on the outward rotating panel and an increase in the TEV/TV vortex loop size. If similar flow structures are present for the gust case, which has forces resembling those of the starting flow, these features would contribute to this enhanced C_L. For the 3c ramp, the 21.5c actuation-out produces a high C_L peak, then the C_L lowers but maintains a larger value than the references cases until the first circulatory recovery peak at ~28.5c traveled. The 50% actuation-out at 22.5c traveled for the 3c ramp occurs just prior to the C_L minimum from the gust. At first it yields a C_L similar to the 21.5c actuation case, but then the C_L is reduced and gradually converges to essentially match the reference cases just prior to the recovery peak. As with the step-up gust cases, tip-panel actuation for the 6c-ramp step-down gust has the smallest effect. For 21.5c actuation-out, the C_L overshoots that of the reference cases initially, then after 2c of further travel the C_L becomes very close to the reference results, within the error. For 50% actuation-out at 24c traversed, there is again an overshoot C_L peak and the C_L during the gust minimum is somewhat higher than that of the fixed-geometry reference cases (and the 21.5c actuation result). The C_L continues to be sustained slightly above all other cases until the recovery peak, but this improvement level remains close to or within the uncertainty. In summary, for the $\mathcal{AR} = 4$ step-down gusts, actuation-out not long before the C_L gust minimum can reduce the magnitude of the drop in lift, and for the 1c and 3c ramps the actuation effect is sustained above the uncertainty until approximately the C_L recovery peak.

The $\mathcal{AR} = 2$ actuation-out results for the step-down gusts are shown in Fig. 7, second row. The rectangular and static-sweep reference cases show more deviation from one another compared to $\mathcal{AR} = 4$, with the static-sweep wing exhibiting reduced C_L after the gust but before the recovery to maximum lift. This is likely due to the relatively greater change in outboard sweep and $\mathcal{AR}$ between the rectangular and static-sweep cases versus $\mathcal{AR} = 4$, but without flow data the exact cause is unknown. Recall that for actuation-out the rectangular and static-sweep geometries represent the states before and after actuation, respectively. For the $\mathcal{AR} = 2$, 1c ramp, the actuation-out at 21.5c reduces the magnitude of the $C_L < 0$ gust peak, similar to $\mathcal{AR} = 4$; just after this, the $\mathcal{AR} = 2$ forces show two positive peaks that again may indicate mechanical backlash. Next, in the C_L recovery before the maximum peak, the actuation-out curve follows both the rectangular and static-sweep cases, then the static-sweep case lags behind the others, until all C_L curves converge at the

maximum recovery peak and remain similar to the end of the motion. This converging behavior also occurs for $\mathcal{AR} = 4$.

For the $\mathcal{AR} = 2$, $3c$ ramp, the $21.5c$ and 50% actuation-out C_L both exhibit overshoot peaks from the initial actuation that are above the reference cases, similar to the $\mathcal{AR} = 4$ wing in terms of timing but relatively larger; the actuation effects persist and reduce the magnitude of the gust minimum. For $\mathcal{AR} = 2$ the C_L increase after the minimum has a higher initial slope for the rectangular and actuation cases (all overlap), compared to $\mathcal{AR} = 4$. Conversely, the $\mathcal{AR} = 2$ static-sweep case shows substantially-reduced C_L in the recovery portion, consistent with the $1c$-ramp gust. Interestingly, the C_L recovery-peak magnitude is slightly larger and occurs earlier for the $21.5c$ actuation-out, versus the other $\mathcal{AR} = 2$ cases. The $\mathcal{AR} = 2$, $6c$-ramp case also shows similar but relatively greater initial C_L overshoot behavior for the actuation cases just after the gust, compared to $\mathcal{AR} = 4$. The $6c$-ramp 50% actuation has a higher slope than all other $6c$ gust cases and therefore a faster initial recovery, but the C_L then reaches a plateau slightly below the maximum value for the reference wings. For $21.5c$ actuation-out, similar to the $3c$-ramp the increasing C_L overlaps at first with the rectangular case, then achieves a higher and earlier C_L maximum, albeit larger than that of the $3c$ ramp. These larger and earlier peaks from $21.5c$ actuation for the $3c$ and $6c$ ramps occur at approximately the same chords traveled as the $\mathcal{AR} = 4$ recovery peaks, perhaps related to the higher $\mathcal{AR}$ achieved near the beginning of the gust.

For the step-down gusts, a summary comparison of the actuation-out effect between $\mathcal{AR} = 4$ and 2 is somewhat confounded by differences in the C_L behavior of the rectangular and static-sweep reference cases for each $\mathcal{AR}$. These aside, the tip-panel actuation-out for both $\mathcal{AR}$s yield similar reductions of the peak magnitude during the C_L minimum from the gust, which is beneficial for gust mitigation. For the two longer ramps, the $\mathcal{AR} = 2$ actuation cases produce relatively larger peaks just after actuation, versus the reference geometries, compared to $\mathcal{AR} = 4$. Further, for $\mathcal{AR} = 2$ the rectangular and actuation cases allow for a faster post-gust recovery (C_L increase) for the $3c$ ramp, and 50% actuation yields a similarly earlier recovery for the $6c$-ramp, not found for $\mathcal{AR} = 4$. Also, for $\mathcal{AR} = 2$ the $21.5c$ actuation generates higher and earlier C_L recovery peaks versus the reference cases, which is not observed for $\mathcal{AR} = 4$. However, for the $1c$-ramp the $\mathcal{AR} = 4$ actuation case results in more sustained C_L between the gust minimum and the recovery peak. Overall, for longer ramps the $\mathcal{AR} = 2$ actuation-out cases are superior for producing higher relative C_L faster, to aid in gust mitigation.

IV. Concluding Remarks

A tip panel with aft-sweep was rotated inward or outward on a low-$\mathcal{AR}$, $\alpha = 45°$ rectanglar main-wing in translation, to study its ability to mitigate lift variations from streamwise gusts of two kinds: step-up and step-down, respectively. Three gust–ramps over distances traveled of $1c$, $3c$, and $6c$ with two actuation timings—near the gust start (21.5c traveled) and at 50% of the ramp distance—were tested for $\mathcal{AR} = 4$ and 2, where the $\mathcal{AR}$ values correspond to the rectangular-wing portion only. The actuation cases were compared to two fixed-geometry references: the rectangular (panel retracted) and static-sweep (panel extended) wings. The C_L definition used both the instantaneous main-wing translation velocity and the variable wing area. The $1c$ step-up gust exhibits unsteady lift behavior similar to that of the $1c$ starting motion, as found by others. For the step-down gusts, the deceleration produces a C_L minimum, then the force recovers to a circulatory peak. Except for the $6c$ step-up gust, all gust cases show a circulatory peak in the post-gust constant-motion part for the rectangular $\mathcal{AR} = 4$ wing. The position and magnitude of this peak coincide across those gust ramp cases when their 50% ramp locations are aligned. The step-down gust force magnitudes are higher than the step-up cases, although the step-up acceleration magnitude is larger than the deceleration for the step-down gusts. Only one value of the tip-panel rotation speed was used, which can be varied in future studies. For this tip rotation speed both inward and outward, the most pronounced effect for $\mathcal{AR} = 4$ was observed for the $1c$-ramp case. Conversely, for $\mathcal{AR} = 2$ the overall greatest tip-actuation influence was found for the $6c$ step-down ramp. For the step-up gusts with actuation-in, the $\mathcal{AR} = 2$ wing produces a greater decrease in C_L but the effect diminishes sooner compared to $\mathcal{AR} = 4$. This may be due to interactions with the more pronounced $\mathcal{AR} = 4$ LEV formation. For both $\mathcal{AR}$s, actuation-in at the 50% ramp distance yields the most sustained reduction in C_L but does not affect the gust peak, whereas the early actuation at $21.5c$ for the $3c$ ramp (and the $6c$ ramp for $\mathcal{AR} = 2$) lowers this peak magnitude. Considering the step-down gusts, for $\mathcal{AR} = 4$ overall the actuation-out increases the C_L compared to the reference cases both during and after the gust, depending on the ramp length. For the longer $3c$ and $6c$ ramps, the $\mathcal{AR} = 2$ actuation-out case generates relatively higher actuation peaks in C_L and the gust recovery is faster, versus $\mathcal{AR} = 4$. For the $1c$ ramp, actuation-out lowers the gust-peak magnitude for both $\mathcal{AR}$s, but the $\mathcal{AR} = 4$ case generates a higher C_L plateau between the gust minimum and the recovery peak. Lastly, the rectangular and static-sweep reference cases have somewhat similar post-gust C_L behavior for the step-up gusts, but this is not true for the $\mathcal{AR} = 4$, $1c$ step-down case and all the $\mathcal{AR} = 2$ step-down gusts.

Acknowledgments

We would like to thank Karan Shah for his assistance with the experimental setup and with acquiring some of the results. This work is supported by the National Science Foundation, award no. CBET-1706453, supervised by Dr. Ronald Joslin.

References

[1] McCroskey, W. J., "Unsteady Airfoils," *Annual Review of Fluid Mechanics*, Vol. 14, No. 1, 1982, pp. 285–311. https://doi.org/10.1146/annurev.fl.14.010182.001441, URL https://doi.org/10.1146/annurev.fl.14.010182.001441.

[2] Dickinson, M. H., and Gotz, K. G., "Unsteady Aerodynamic Performance of Model Wings at Low Reynolds Numbers," *Journal of Experimental Biology*, Vol. 174, No. 1, 1993, pp. 45–64. URL http://jeb.biologists.org/content/174/1/45.

[3] Taira, K., and Colonius, T., "Three-dimensional flows around low-aspect-ratio flat-plate wings at low Reynolds numbers," *Journal of Fluid Mechanics*, Vol. 623, 2009, p. 187–207. https://doi.org/10.1017/S0022112008005314.

[4] Jardin, T., Farcy, A., and David, L., "Three-dimensional effects in hovering flapping flight," *Journal of Fluid Mechanics*, Vol. 702, 2012, p. 102–125. https://doi.org/10.1017/jfm.2012.163.

[5] Stevens, P. R. R. J., Babinsky, H., Manar, F., Mancini, P., Jones, A. R., Nakata, T., Phillips, N., Bomphrey, R. J., Gozukara, A. C., Granlund, K. O., and Ol, M. V., "Experiments and Computations on the Lift of Accelerating Flat Plates at Incidence," *AIAA J.*, Vol. 55, No. 10, 2017, pp. 3255–3265.

[6] Lentink, D., and Dickinson, M. H., "Rotational accelerations stabilize leading edge vortices on revolving fly wings," *J Expl Biol.*, Vol. 212, 2009, pp. 2705–2719.

[7] Kruyt, J. W., van Heijst, G. F., Altshuler, D. L., and Lentink, D., "Power Reduction and the Radial Limit of Stall Delay in Revolving Wings of Different Aspect Ratio," *J. R. Soc. Interface*, Vol. 12, 2015, p. 20150051.

[8] Wolfinger, M., and Rockwell, D., "Flow structure on a rotating wing: effect of radius of gyration," *Journal of Fluid Mechanics*, Vol. 755, 2014, p. 83–110. https://doi.org/10.1017/jfm.2014.383.

[9] Lee, Y. J., Lua, K. B., and Lim, T. T., "Aspect Ratio Effects on Revolving Wings with Rossby Number Consideration," *Bioinspir. Biomim.*, Vol. 11, No. 5, 2016, p. 056013.

[10] Jardin, T., and Colonius, T., "On the Lift-Optimal Aspect Ratio of a Revolving Wing at Low Reynolds Number," *J. R. Soc. Interface*, Vol. 15, No. 143, 2018.

[11] Bhat, S. S., Zhao, J., Sheridan, J., Hourigan, K., and Thompson, M. C., "Uncoupling the effects of aspect ratio, Reynolds number and Rossby number on a rotating insect-wing planform," *Journal of Fluid Mechanics*, Vol. 859, 2019, p. 921–948. https://doi.org/10.1017/jfm.2018.833.

[12] Harbig, R. R., Sheridan, J., and Thompson, M. C., "Reynolds number and aspect ratio effects on the leading-edge vortex for rotating insect wing planforms," *Journal of Fluid Mechanics*, Vol. 717, 2013, p. 166–192. https://doi.org/10.1017/jfm.2012.565.

[13] Jones, A. R., Pitt Ford, C. W., and Babinsky, H., "Three-Dimensional Effects on Sliding and Waving Wings," *J. Aircraft*, Vol. 48, No. 2, 2011, pp. 633–644.

[14] Hartloper, C., Kinzel, M., and Rival, D. E., "On the competition between leading-edge and tip-vortex growth for a pitching plate," *Experiments in Fluids*, Vol. 54, No. 1, 2013, p. 1447. https://doi.org/10.1007/s00348-012-1447-5, URL https://doi.org/10.1007/s00348-012-1447-5.

[15] Beem, H. R., Rival, D. E., and Triantafyllou, M. S., "On the stabilization of leading-edge vortices with spanwise flow," *Experiments in Fluids*, Vol. 52, No. 2, 2012, pp. 511–517. https://doi.org/10.1007/s00348-011-1241-9, URL https://doi.org/10.1007/s00348-011-1241-9.

[16] Wong, J. G., Kriegseis, J., and Rival, D. E., "An Investigation Into Vortex Growth and Stabilization for Two-Dimensional Plunging and Flapping Plates with Varying Sweep," *Journal of Fluids and Structures*, Vol. 43, 2013, pp. 231–243.

[17] Wong, J., and Rival, D., "Determining the relative stability of leading-edge vortices on nominally two-dimensional flapping profiles," *Journal of Fluid Mechanics*, Vol. 766, 2015, p. 611–625. https://doi.org/10.1017/jfm.2015.39.

[18] Jardin, T., and David, L., "Spanwise gradients in flow speed help stabilize leading-edge vortices on revolving wings," *Phys. Rev. E*, Vol. 90, 2014, p. 013011. https://doi.org/10.1103/PhysRevE.90.013011, URL https://link.aps.org/doi/10.1103/PhysRevE.90.013011.

[19] Klaassen van Oorschot, B., Mistick, E. A., and Tobalske, B. W., "Aerodynamic consequences of wing morphing during emulated take-off and gliding in birds," *Journal of Experimental Biology*, Vol. 219, No. 19, 2016, pp. 3146–3154. https://doi.org/10.1242/jeb.136721, URL http://jeb.biologists.org/content/219/19/3146.

[20] Hayostek, S., Amitay, M., Zhang, K., Taira, K., He, W., and Theofilis, V., "Wake Dynamics of Finite Aspect Ratio Wings Part 1: An Experimental Study," *AIAA Paper 2019-1384*, 2019, pp. 1–13.

[21] Zhang, K., Taira, K., Hayostek, S., Amitay, M., He, W., and Theofilis, V., "Wake Dynamics of Finite Aspect Ratio Wings Part II: Computational Study," *AIAA Paper 2019-1385*, 2019, pp. 1–10.

[22] Chowdhury, J., Cook, L., and Ringuette, M. J., "The Vortex Formation of an Unsteady Translating Plate with a Rotating Tip," *AIAA Paper 2019-0348*, 2019, pp. 1–19.

[23] Medina, A., Rockwood, M., Garmann, D. J., and Visbal, M. R., "Integration of Experiments and Computations of Swept-Wing Dynamic Stall," *AIAA Paper 2019-2324*, 2019, pp. 1–18.

[24] Nikolic, V. R., "Optimal Movable Wing Tip Strake," *Journal of Aircraft*, Vol. 48, No. 1, 2011, pp. 335–341. https://doi.org/10.2514/1.c031014, URL https://doi.org/10.2514/1.C031014.

[25] Lee, T., and Pereira, J., "Modification of static-wing tip vortex via a slender half-delta wing," *Journal of Fluids and Structures*, Vol. 43, 2013, pp. 1 – 14. https://doi.org/https://doi.org/10.1016/j.jfluidstructs.2013.08.004, URL http://www.sciencedirect.com/science/article/pii/S0889974613001722.

[26] Reynolds, K. V., Thomas, A. L. R., and Taylor, G. K., "Wing Tucks Are a Response to Atmospheric Turbulence in the Soaring Flight of the Steppe Eagle *Aquila nipalensis*," *J. R. Soc. Interface*, Vol. 11, No. 20140645, 2014, pp. 1–11.

[27] Wang, S., Zhang, X., He, G., and Liu, T., "Lift Enhancement by Bats? Dynamically Changing Wingspan," *J. R. Soc. Interface*, Vol. 12, No. 20150821, 2015, pp. 1–11.

[28] Harvey, C., Baliga, V. B., Lavoie, P., and Altshuler, D. L., "Wing Morphing Allows Gulls to Modulate Static Pitch Stability During Gliding," *J. R. Soc. Interface*, Vol. 16, No. 20180641, 2019, pp. 1–8.

[29] Chin, D. D., Matloff, L. Y., Stowers, A. K., Tucci, E. R., and Lentink, D., "Inspiration for Wing Design: How Forelimb Specialization Enables Active Flight in Modern Vertebrates," *J. R. Soc. Interface*, Vol. 14, No. 20170240, 2017, pp. 1–18.

[30] Wibawa, M., Steele, S. C., Dahl, J. M., Rival, D. E., Weymouth, G. D., and Triantafyllou, M. S., "Global vorticity shedding for a vanishing wing," *J. Fluid Mech.*, Vol. 695, 2012, pp. 112–134.

[31] Steele, S. C., Dahl, J. M., Weymouth, G. D., and Triantafyllou, M. S., "Shape of Retracting Foils That Model Morphing Bodies Controls Shed Energy and Wake Structure," *J. Fluid Mech.*, Vol. 805, 2016, pp. 355–383.

[32] Scofield, T., Jia, K., Wei, M., and Bhattacharya, S., "Vorticity-Transfer in a Leading-Edge-Vortex due to Controlled Spanwise-Bending," *AIAA Paper 2019-2161*, 2019, pp. 1–12.

[33] Di Luca M, H. G. N. F., Mintchev S, and D, F., "Bioinspired morphing wings for extended flight envelope and roll control of small drones," *Interface Focus*, Vol. 20160092, 2017. https://doi.org/10.1098/rsfs.2016.0092.

[34] Granlund, K., Monnier, B., Ol, M., and Williams, D., "Airfoil Longitudinal Gust Response in Separated vs. Attached Flows," *Phys. Fluids*, Vol. 26, 2014, p. 027103.

[35] Greenblatt, D., M$'$ueller-Vahl, H., Strangfeld, C., Medina, A., Ol, M. V., and Granlund, K. O., "High Advance-Ratio Airfoil Streamwise Oscillations: Wind Tunnel vs. Water Tunnel," *AIAA Paper 2016-1356*, 2016, pp. 1–19.

[36] Medina, A., Ol, M. V., Greenblatt, D., M$'$ueller-Vahl, H., and Strangfeld, C., "High-Amplitude Surge of a Pitching Airfoil: Complementary Wind- and Water-Tunnel Measurements," *AIAA Journal*, Vol. 56, No. 4, 2018, pp. 1703–1709.

[37] Mulleners, K., Mancini, P., and Jones, A. R., "Flow Development on a Flat-Plate Wing Subjected to a Streamwise Acceleration," *AIAA J.*, Vol. 55, No. 6, 2017, pp. 2118–2122.

[38] Marzanek, M. F., and Rival, D. E., "Separation mechanics of non-slender delta wings during streamwise gusts," *Journal of Fluids and Structures*, Vol. 90, 2019, pp. 286 – 296. https://doi.org/https://doi.org/10.1016/j.jfluidstructs.2019.07.001, URL http://www.sciencedirect.com/science/article/pii/S088997461930132X.

[39] Slaouti, A., and Gerrard, J. H., "An experimental investigation of the end effects on the wake of a circular cylinder towed through water at low Reynolds numbers," *Journal of Fluid Mechanics*, Vol. 112, 1981, p. 297–314. https://doi.org/10.1017/S0022112081000414.

[40] Mueller, T. J., and DeLaurier, J. D., "Aerodynamics of Small Vehicles," *Annual Review of Fluid Mechanics*, Vol. 35, 2003, pp. 89–111.

[41] Lisoski, D. L. A., "Nominally 2-Dimensional Flow About a Normal Flat Plate," Ph.D. thesis, California Institute of Technology, 1993.

[42] Ol, M., and Babinsky, H., "Extensions of fundamental flow physics to practical MAV aerodynamics," Tech. Rep. TR-AVT-202, NATO STO, 2016. Ol and Babinsky are Co-Chairs.

[43] Dickson, W. B., and Dickinson, M. H., "The effect of advance ratio on the aerodynamics of revolving wings," *Journal of Experimental Biology*, Vol. 207, No. 24, 2004, pp. 4269–4281. https://doi.org/10.1242/jeb.01266, URL http://jeb.biologists.org/content/207/24/4269.

[44] Harbig, R. R., Sheridan, J., and Thompson, M. C., "The role of advance ratio and aspect ratio in determining leading-edge vortex stability for flapping flight," *Journal of Fluid Mechanics*, Vol. 751, 2014, p. 71–105. https://doi.org/10.1017/jfm.2014.262.

[45] Johnson, W., *Helicopter Theory*, Dover Books on Aeronautical Engineering, Dover Publications, Newburyport, 2012.

[46] Jardin, T., "Coriolis Effect and the Attachment of the Leading Edge Vortex," *J. Fluid Mech.*, Vol. 820, 2017, pp. 312–340.